J Solid State Electrochem (2012) 16:1605–1613
DOI 10.1007/s10008-011-1563-9

ORIGINAL PAPER

Effect of preparative methods on electrical and electrochemical performance of lanthanum strontium manganite

K. R. Nagde · S. S. Bhoga

Received: 25 June 2011 / Revised: 22 September 2011 / Accepted: 23 September 2011 / Published online: 14 October 2011

Abstract The electrochemical performance of $La_{0.8}Sr_{0.2}MnO_3$: $Ce_{0.8}Gd_{0.2}O_2$ composite cathode was investigated for solid oxide fuel cell applications. Sol–gel, combustion, and solid-state syntheses yielded rhombohedral $La_{0.8}Sr_{0.2}MnO_3$, whereas mechanochemical process gave cubic structure. X-ray diffraction results established good chemical stability of $La_{0.8}Sr_{0.2}MnO_3$ with $Ce_{0.8}Gd_{0.2}O_2$ composite cathode. Combustion synthesis was found best among all preparative methods on the basis of lowest area specific resistance 0.70 Ω cm^2 at 800 °C. The activation energy E_a=1.09±0.01 eV indicated absorption of O_2 and was the rate-limiting process of cathode.

Keywords SOFC · Composite cathode · X-ray powder diffraction · Electrical conductivity · Electrochemical impedance spectroscopy

Introduction

Perovskites exhibit oxygen non-stoichiometry depending on composition, temperature, and oxygen partial pressure. The $LaMnO_3$, LM, with perovskite structure can tolerate a considerable portion of vacancies at the La^{3+} site giving rise to compositions of $La_{(1-\delta)}MnO_3$ type with the charge compensated by the conversion of Mn^{3+} to Mn^{4+} [1]. Lanthanum strontium manganite, LSM, has been considered as one of the most promising cathode materials for solid oxide fuel cell (SOFC) applications due to its high electrode activity for the oxygen reduction reaction, high electronic conductivity, and chemical as well as mechanical compatibility with the established solid electrolytes [2].

Cathode over-potential has been considered as one of the major factors in evaluating performance of SOFC. In this regard, commonly used means for improving the electrochemical performance has been the addition of oxyion conducting second phase to the electronically conducting electrode material called composite [3]. Composite cathodes exhibit much lower over-potentials than single-phase by virtue of parallel paths for ionic and electronic charge carriers [4]. The use of the composite cathode, has allowed spreading of the electrochemical reaction zone from the electrode/electrolyte interface into the electrode. The chemical reactivity between LSM and yttria-stabilized zirconia, YSZ, leads to the formation of undesired pyrochlore La_2ZrO_7 phase in case of LSM–YSZ composite cathodes [5]. On the other hand, it has been shown that gadolia-doped ceria, GDC, has edge over YSZ electrolyte because of following reasons [3]: (1) Its higher ionic conductivity as compare to YSZ, (2) lower interfacial resistance of LSM–GDC interface than LSM–YSZ interface, and (3) no reaction between doped ceria and LSM at high temperatures. In fact, the microstructural features, including the porosity, grain size, and nature of grain-boundary, which depend on the process, play the vital role in the performance of cathode.

In the light of aforementioned facts, the present study was aimed at preparing LSM via various techniques viz, combustion, sol–gel, solid-state reaction (SSR), and mechanochemical to optimize preparative technique to obtain

K. R. Nagde · S. S. Bhoga (✉)
Department of Physics, RTM Nagpur University,
Nagpur 440033 Maharashtra, India
e-mail: msrl.physics1@gmail.com

improved electrochemical performance of LSM–GDC composite.

Experimental

All initial reagents (purity ≅ 99.9%) used during present study were procured from Aldrich (USA). Prior to the weighing, the reagents were dried at 120 °C for 6 h in order to remove the traces of moisture present. The $La_{0.8}Sr_{0.2}MnO_3$, LSM, was prepared using combustion technique as described elsewhere [6]. Other techniques used for the preparation of LSM are described below:

Sol–gel synthesis

The $La(NO_3)_3{\cdot}6H_2O$, $Mn(NO_3)_2{\cdot}6H_2O$, and $Sr(NO_3)_2$ precursors were taken as reagents. Ethylenediaminetetraacetic acid (EDTA) and citric acid were used as polymerization and complexation agents, respectively. Metal ion to EDTA to citric acid mole ratio was taken as 1:1:1.5. The metallic salts solution was prepared by adding stoichiometric amount of metal ions into the distilled water. The solution of salts, thus obtained, was then added into 300 ml solution of citric acid (15 g) and EDTA. The pH was maintained at 6 so as to obtain the homogeneous solution. The solution was then heated to 150 °C using hot plate while stirring constantly for the formation of homogeneous sol. The sol was then heated to 350 °C so as to remove the excess of solvent to yield intermediate resin. Finally, the resin was calcined at 500 °C in air. The calcined powder was pressed uniaxially at 4 t/cm^2 using Specac (UK) hydraulic press and die-punch to obtain pellets of dimensions 9 and 1–2 mm diameter and thickness, respectively. The pellets were then sintered at 800 °C for 4 h.

Solid-state reaction

The stoichiometric mixture of well-dried reagents La_2O_3, $SrCO_3$, and $MnCO_3$ was ground using Pulversitte-6 planetary mono-mill at the rate of 300 rpm (rotation per minute) under acetone medium for 4 h. The resulted well-ground powder was then pelletized as described above and sintered at 1,300 °C for 4 h.

Mechanochemical synthesis

The La_2O_3 was initially heated at 1,000 °C for 12 h so as to remove absorbed H_2O and CO_2 before weighing. On the other hand, MnO_2 was heated at 600 °C for 12 h in order to convert it into Mn_2O_3 [7]. Prior to the weighing SrO was dried at 120 °C for 4 h. The dried SrO was weighed by taking it in dry ampoule, which was sealed. Later, the reactants La_2O_3, Mn_2O_3, MnO_2, and SrO were mixed in an appropriate stoichiometric ratio as per reaction (1) given below.

$$0.4(La_2O_3 + Mn_2O_3) + 0.2(SrO + MnO_2) \rightleftarrows La_{0.8}\,Sr_{0.2}\,MnO_3 \quad (1)$$

The above-mentioned mixture was taken in 80 ml WC (tungsten carbide) bowl loaded with 35 balls of 10 mm diameter, and milled for 3 h at the rate of 600 rpm. The stearic acid was used as a process control agent (PCA). Finally, the ground sample, in the form of pellets, was sintered at 700 °C for 4 h.

The $Ce_{0.8}Gd_{0.2}O_2$, GDC, nano-powder procured from Aldrich (USA) was used as an electrolyte. Initially, combustion-derived LSM, selected on the basis of highest DC conductivity among all the preparative methods, was used as electronic conductor to optimize LSM–GDC composite cathode composition. Later, the 70LSM:30GDC was taken to study the effect of preparative methods of LSM on the electrochemical performance of composite cathode. Each composite mixture was ball milled at the rate of 300 rpm for 1 h under acetone as discussed above. Finally, the pellets of well-ground composite mixture were sintered at 1,000 °C for 4 h.

For electrochemical investigations, initially the slurry/ink of each composite cathode (LSM prepared by different techniques) were obtained as follows. The mixture of 1 g of 70LSM:30GDC composite with 3 wt.% polyvinyl buteral binder, 25 wt.% sodium free corn oil, and methyl ethyl ketone was ball milled for 5 h at the rate of 300 rpm. The GDC nano-powder was fired at 800 °C for 2 h. Subsequently, they, in the form of circular disks of 9 and 1–2 mm diameter and thickness, respectively, were sintered at 1,400 °C for 6 h. The density of sintered pellet was about 96% of the theoretical value. Both the flat surfaces of the disk were then roughened with #60 grid paper and cleaned with an acetone. The slurry/ink of cathode material was then spin coated on both the flat surfaces of sintered GDC electrolyte revolving at the rate of 3,000 rpm for 60 s so as to obtain the symmetric cells of configuration given below,

$$\text{Pt/composite cathode/GDC/composite cathode/Pt} \quad (2)$$

The symmetric cells were initially baked at 600 °C for 2 h so as to burn out the organic binders, and then finally sintered at 1,000 °C for 2 h. The details of symmetric cells are summarized in Table 1.

All the samples under study were characterized using X-ray powder diffraction, PANalytical X'pert PRO, Philips, Holland, with curved graphite crystal as a monochromator, and using CuK_α radiations. The obtained XRD data were profile fitted with the help of X'pert Highscore plus software before indexing. The values of d and relative

Table 1 Details of preparative techniques of LSM used to obtain 70LSM/30GDC composite, cell abbreviations and activation energies of symmetric cells

Preparative technique of LSM	LSM abbreviation	Cell abbreviation	E_a (eV)	$E_{a'}$ (eV)
Combustion	LSM(comb)	Cell(comb)	1.09±0.01	1.00±0.03
Sol–gel	LSM(sol–gel)	Cell(sol–gel)	2.10±0.03	1.99±0.01
Solid-state reaction	LSM(SSR)	Cell(SSR)	1.40±0.01	1.38±0.01
Mechanochemical	LSM(mechano)	Cell(mechano)	1.15±0.01	1.20±0.01

$E_{a'}$ activation energy determined from temperature-dependent peak frequency plots

intensity (I/I_0) for LSM obtained with the help of X-pert Highscore plus, and then compared with the standard Joint Committee on Powder Diffraction Standard (JCPDS) data. Also, the lattice cell constants were determined using unit cell, computer software developed by Holland and Redfern [8]. The mean deviation in lattice cell constants obtained from Eq. 3

$$\Delta_{\text{cell}} = \frac{\sqrt{\left(a_{\text{exp}} - a_{\text{JCPDS}}\right)^2 + \left(b_{\text{exp}} - b_{\text{JCPDS}}\right)^2 + \left(c_{\text{exp}} - c_{\text{JCPDS}}\right)^2}}{3} \tag{3}$$

where, a, b, and c are lattice cell constants. The crystallite size was determined using X'pert Highscore plus based on Debye Scherer formula (4),

$$t = \frac{0.9\lambda}{\beta \cos\theta_\beta} \tag{4}$$

where t, λ, and θ_B are thickness of crystallite, X-ray wavelength, and Bragg's angle, respectively. Here, β was obtained using formula

$$\beta = \beta_m^2 - \beta_s^2 \tag{5}$$

where, β_m and β_s were measured and standard full width of half maxima (FWHM) of diffracted line, respectively. The β_s was estimated from the XRD pattern obtained by running the experiment on the standard silicon sample provided by Panalytical, Netherlands.

The microstructures of sintered samples were examined with the help of scanning electron microscope, JEOL JSM-6380A. The density of the sintered pellets was measured following Archimedes principle using Mettler XS105 dual-range monopan balance with density kit attachment, and built-in density measurement software. The oxygen stoichiometry was determined using iodometric titration [9]. The microhardness was determined using Shimadzu (Japan) microhardness tester.

The experimental procedures followed to determine DC conductivity as a function of temperature, and to evaluate electrochemical performance of composite cathode were similar to those described elsewhere [10].

Results and discussion

X-ray powder diffraction

X-ray powder diffraction patterns of LSM prepared by different techniques are shown in Fig. 1 (a–d). As seen all the diffracted peaks (Fig. 1 (a–c)) matched well with the standard JCPDS data corresponding to rhombohedral LSM (file no. 00-047-0444 of $La_{0.9}Sr_{0.1}MnO_3$). It is worth to mention here that JCPDS data of orthorhombic or tetragonal $La_{0.8}Sr_{0.2}MnO_3$ did not match with any experimental XRD patterns. On the other hand, all the diffracted characteristic peaks appeared in Fig. 1 (d) were in good agreement with the JCPDS data due to the cubic LM (file no. 01-075-0440 ($LaMnO_3$)) rather than that of rhombohedral lattice. Additionally, the lattice parameters (Table 2) determined experimentally matched well with the standard JCPDS values. The splitted (111) reflection (Fig. 1 (a–c)) confirmed the formation of rhombohedral LSM. Harwood has also observed splitted (111) reflection in case of $LaMnO_3$ [11]. According to him a split in (111) reflection cannot be obtained in orthogonal unit cell, and hence, the possibility of tetragonal and orthorhombic structure was eliminated. Hence, the LSM prepared by mechanochemical method was of cubic structure. Absence of any peak corresponding to the reagents in all the cases, Fig. 1 (a–d), suggested the formation of single-phase rhombohedral and cubic LSM, respectively. From the above results it can be inferred that the 3-h dry mixing in presence of stearic acid was sufficient for the formation of LSM, which is lesser as compared to the 7 h required for the simple dry mixing without PCA [7]. Among all the preparative methods, mechanochemical synthesis required lowest sintering temperature (700 °C) for the formation of single-phase LSM. Sol–gel-derived powder formed single-phase LSM after sintering at 800 °C while combustion and solid-state reaction techniques required relatively higher sintering temperatures 1,000 and 1,300 °C, respectively.

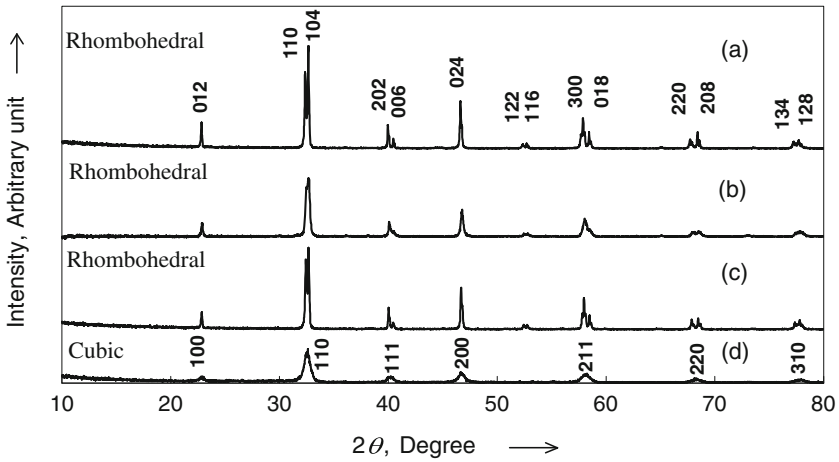

Fig. 1 The X-ray powder diffraction patterns of LSM prepared by *a* combustion, *b* sol–gel, *c* solid-state reaction, and *d* mechanochemical synthesis

A close scrutiny of the Table 2 suggested that the sintered density of LSM prepared by combustion and solid-state reaction was higher as compared to it prepared by sol–gel and mechanochemical routes. As expected, the microhardness, HV number, increased with an increased sintered density. A close look at Table 2 also revealed that the combustion-derived LSM gave exact oxygen stoichiometry. On the other hand, mechanochemical synthesis resulted oxygen-deficient LSM. The oxygen deficiency is due to reduction of manganese accompanied by the formation of oxygen vacancies. In contrast, oxygen excess LSM is due to the oxidation of Mn and the formation of equal amounts of cation vacancies on both cation sublattices so as to achieve charge neutrality. As a matter of fact, the stoichiometry and, therefore, the symmetry of the crystal structure of the LM are very sensitive to the preparative procedure [12]. Accordingly, the number of Mn^{4+} in the LSM oxides is not only fixed by the introduction of a certain amount of non-stoichiometry, but also depends on firing atmosphere, temperature, and time [13]. The observed difference in the lattice cell constants (Table 2) is attributed to the variation in Mn^{4+} content of LSM prepared by different preparative routes.

The X-ray powder diffraction patterns of composite cathode (70LSM:30GDC) unsintered and sintered at 1,000 °C for 4 h are shown in Fig. 2 (a) and (b), respectively. The presence of broadened peaks corresponding to both the LSM and GDC indicated submicron-sized grains. The obtained crystallite sizes were 401.00±2.1 and 349.25±1.8 nm, respectively. Furthermore, the intensity of all the diffracted peaks (Fig. 2 (b)) not only increased but also reduced the FWHM after sintering the composite at 1,000 °C for 4 h. Consequently, the crystallite size of the LSM and GDC increased (440.00±1.5 nm (LSM) and 466.25±1.2 nm (GDC)) after sintering the composite at 1,000 °C for 4 h. The increased grain size after sintering is in good agreement with the general observation. It is worth to mention here that, no line(s) corresponding to any intermediate phase due to chemical reaction between LSM and GDC are seen. These results implied good chemical stability of LSM and GDC on ball milling (4 h) and subsequently sintering them at 1,000 °C for 4 h. It can be, thus, said that the cathode under study is only a physical mixture of LSM and GDC and so composite.

Table 2 A comparison of lattice cell constants, crystallite size (c_s), microhardness number (HV), relative sintered density (ρ), and oxygen stoichiometry (δ) of LSM prepared by different techniques

Type of LSM	Crystal structure	Lattice cell constants			c_s (Å)	HV	ρ (%)	δ (±0.02)
		a (Å)	*c* (Å)	*v* (Å^3)				
LSM(comb)	Rhombohedral	5.220±0.09	13.719±0.02	342.867±0.02	4,257±9	350±3	90.0±1.2	0.010
LSM(sol–gel)	Rhombohedral	5.528±0.01	13.369±0.04	353.880±0.01	903±3	167±2	75.79±0.9	0.115
LSM(SSR)	Rhombohedral	5.520±0.03	13.368±0.02	352.847±0.05	3,334±8	281±3	84.83±1.0	0.145
LSM(mechano)	Cubic	3.887±0.01	–	58.765±0.01	130±1	114±1	71.11±1.8	−0.102
JCPDS(047–0444)	Rhombohedral	5.533	13.356	354.18	–	–	–	–
JCPDS(075–0440)	Cubic	3.880	–	58.41	–	–	–	–

Δ_{cell} mean deviation corresponding to lattice cell constants, *HV* microhardness number, c_s crystallite size

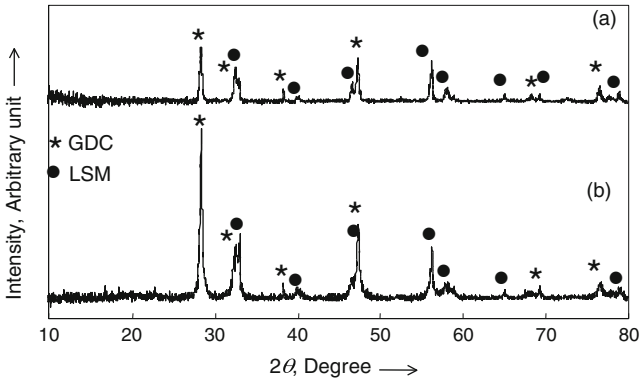

Fig. 2 The X-ray powder diffraction patterns of composite 70LSM:30GDC *a* unsintered and *b* sintered at 1,000 °C for 4 h

Scanning electron microscopy

Scanning electron microphotographs of LSM prepared by combustion, sol–gel, solid-state reaction, and mechanochemical synthesis are given in Fig. 3a–d, respectively. A comparative study of figures revealed largest grain size of combustion-derived LSM as compared to those of it prepared by other techniques. A close look at Fig. 3d also revealed that the effective grain size of mechanochemically prepared LSM was in the submicron range.

The SEM photograph of cathode surface of Cell (comb) (shown in Fig. 4a) revealed agglomerated submicron-sized grains with a large number of pores of submicron size. As seen in Fig. 4b the composite electrode and electrolyte form intimate contact across the interface. Moreover, the electrode/electrolyte interface was homogeneous. Despite thermal cycles at 800 °C neither cracks nor separations between the electrode and electrolyte was found at the interface. The electrode layer thickness was approximately 7.60 μm.

DC conductivity

The plots of log σT versus $10^3/T$ for the LSM prepared by different techniques are depicted in Fig. 5. In general, all the samples obeyed a well-known Arrhenius law (Fig. 5) below 680 °C.

$$\sigma T = A \exp\left(\frac{-E_a}{kT}\right) \tag{6}$$

where A is pre-exponential factor, E_a is the activation energy for conduction, and k is Boltzman constant. The enhancement in conductivity is attributed to increased charge carrier (polarons) concentration due to temperature-dependent Mn^{3+} to Mn^{4+} conversion. A close scrutiny of the Fig. 5 revealed lowest conductivity as well as activation energy for mechanochemically derived LSM. In contrast, highest conductivity observed for combustion-derived LSM among all. The lowest conductivity in mechanochemically prepared LSM is due to pores that resulted from agglomerated submicron-sized grains (Fig. 3d). The lower conductivity in mechanochemically prepared cathode compared to it prepared by other methods has also been reported in case of $Nd_{1.8}Ce_{0.2}CuO_4$ [14]. A semiconductor to pseudo-metal phase transition was around 680 °C (shown by vertical line) in almost all the samples (Fig. 5). Tsipis et al. have also

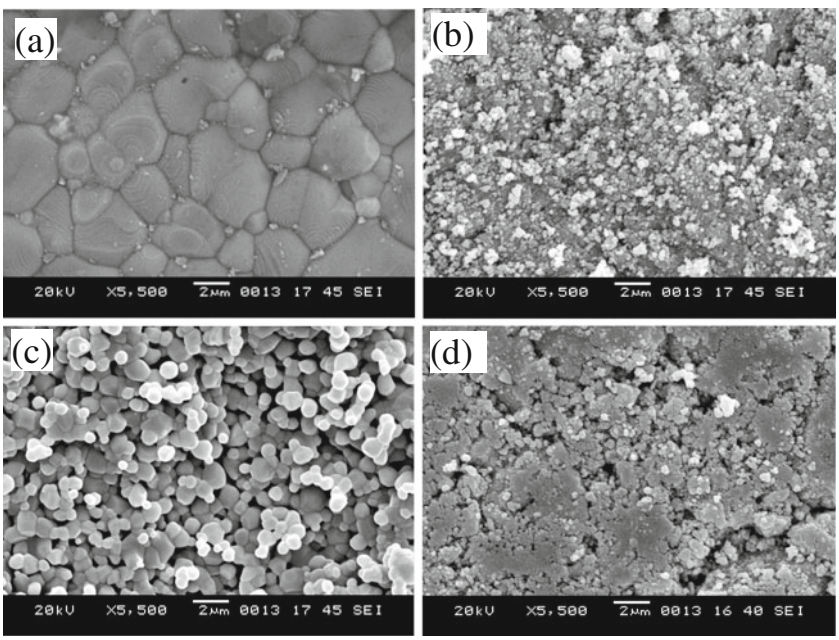

Fig. 3 Scanning electron microphotographs of LSM prepared by **a** combustion, **b** sol–gel, **c** solid-state reaction, and **d** mechanochemical syntheses

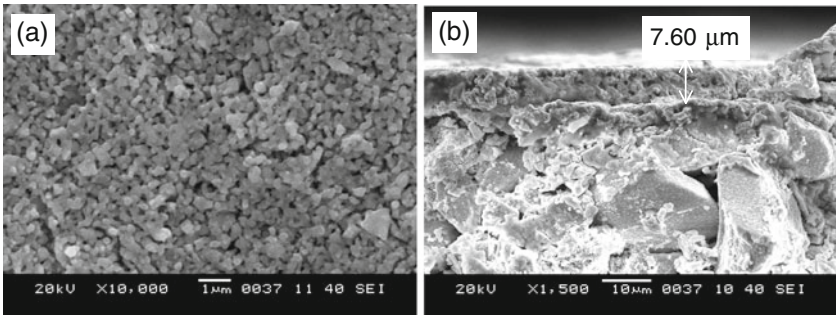

Fig. 4 Scanning electron micrographs of cathode surface of **a** Cell(comb) and **b** electrode/electrolyte interface of Cell(comb)

reported such phase transition in LSM at 680 °C [15]. At high temperatures, release of lattice oxygen reduced charge $2(h^{\bullet})$ carrier density according to reaction (7) given below [16].

$$2h^{\bullet} + O_O^X \rightleftarrows V_O^{\bullet\bullet} + \frac{1}{2}O_2 \tag{7}$$

The conductivity, thus, reduced with an increased temperature beyond 680 °C. Among all, the combustion-derived LSM was chosen on the basis of highest conductivity and lowest activation enthalpy for further study.

The variation of electrical conductivity of combustion-derived LSM with change in oxygen partial pressure at 600 and 700 °C is shown in Fig. 6. A linear dependence of conductivity on oxygen partial pressure (Fig. 6), within the range of measurement, is due to change in defect structure. Similar results have also been reported for undoped

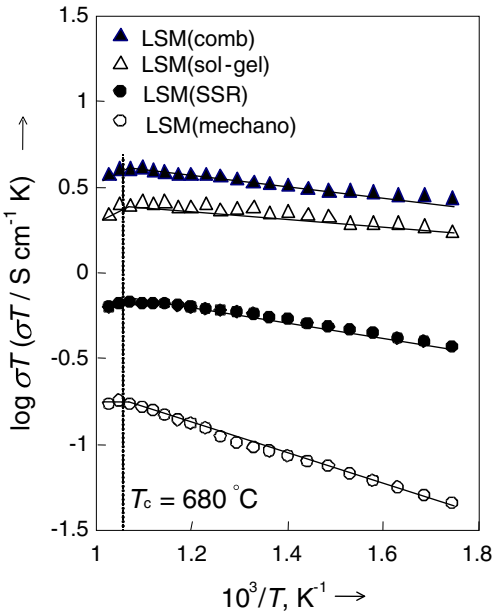

Fig. 5 Arrhenius plots of the total conductivity of LSM prepared by different techniques

$LaMnO_3$ [17]. The defect reaction for $La_{1-x}Sr_xMnO_{3-\delta}$ may be represented by [17]

$$2Mn_{Mn}^{\bullet} + O_O^x \rightleftarrows 2Mn_{Mn}^{x} + V_O^{\bullet\bullet} + \frac{1}{2}O_2 \tag{8}$$

Sr-doped $LaMnO_3$ was, generally, considered as a p-type semiconductor exhibiting both Mn^{3+} and Mn^{4+} ions. Their corresponding ratio depended on oxygen partial pressure and temperature. The charge neutrality condition for Sr-doped $LaMnO_3$ is expressed as [18]

$$\left[Sr_{La}^{'}\right] + 3\left[V_{La}^{'''}\right] + 3\left[V_{Mn}^{'''}\right] + n \rightleftarrows \left[V_O^{\bullet\bullet}\right] + p \tag{9}$$

where $Sr_{La}^{'}$ denotes Sr^{2+} ions introduced into La^{3+} lattice sites, $V_{La}^{'''}$ and $V_{Mn}^{'''}$ are cation vacancies, $V_O^{\bullet\bullet}$ oxygen vacancy and n and p are the concentrations of electron and hole, respectively.

Electrochemical impedance spectroscopy

Typical complex impedance plots for Cell(comb) at different temperatures are depicted in Fig. 7. In general, the convoluted impedance plots are seen. The presence of two semicircular arcs (dotted curves in the low- and the mid-frequency regimes) suggested at least two different electrode processes that limited the oxygen reduction reaction. Absence of semicircular arc in the high-frequency regime was due to the high-frequency limitation of FRA 1255B (1 MHz). A close scrutiny of Fig. 7 also revealed that the real axis intercept of semicircular arc increased with the reduction in temperature implying increased resistance of electrolyte as well as electrode. As a matter of fact, at cathode oxygen reduces by accepting electrons to give oxyion. This cathodic reaction requires gaseous oxygen and good electronic conductivity in the electrode material. In addition to these, the possibility for created oxide ions to be transported away from the reaction site into the bulk of the electrolyte is

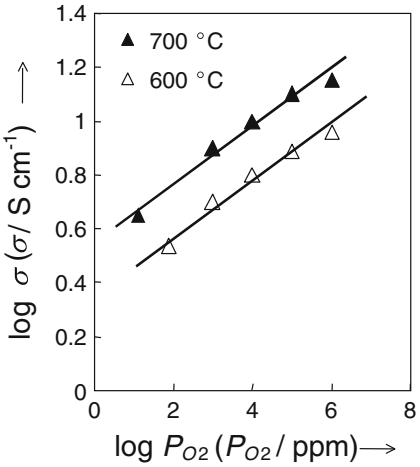

Fig. 6 Variation of conductivity of LSM with oxygen partial pressure at 600 and 700 °C

necessary. These criteria are fulfilled in the vicinity of the TPB, triple-phase boundary, between electrode, electrolyte, and air.

An electrical equivalent circuit representing complex impedance behavior is shown as insert of Fig. 7. The inductor was accounted for the connecting leads during the measurements. The R_{bulk} in parallel with C_1 was the bulk resistance due to GDC electrolyte; whereas, C_1 represented the displacement current through the electrolyte. R_2 and R_1 were the resistances corresponding to low- and mid-frequency semicircles, respectively. Here *CPE*, C_{dl}, and W represented the constant phase element, double layer capacitance, and Warburg impedance, respectively [19].

The ASR was evaluated from low (R_2) and mid-frequency (R_1) semicircular arcs for the Cell(comb) using equation given below

$$\mathrm{ASR} = \left(\frac{R_1 + R_2}{2}\right) \times S \tag{10}$$

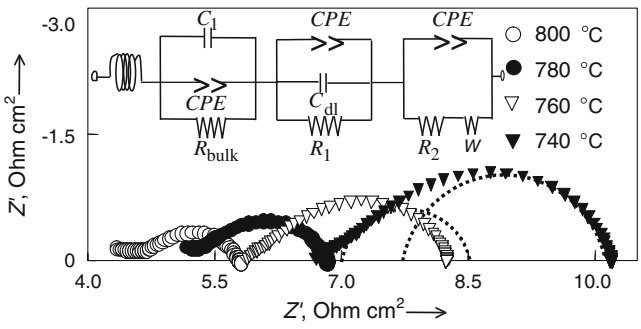

Fig. 7 Complex impedance plots of Cell(comb) at different temperatures

where S is the surface area of the electrolyte–electrode interface. Suzuki et al. have also evaluated ASR from mid- and low-frequency semicircular arcs [20].

The variation of peak frequency (f_p) corresponding to the low-frequency semicircle in complex impedance plane with temperature, depicted in Fig. 8, suggested Arrhenius-like behavior. The activation energy (E_a) was determined using Eq. 11

$$f_p = f_0 \ \exp\left(\frac{-E_a}{kT}\right) \tag{11}$$

where, f_p and f_0 are jump and attempt frequencies, respectively. A comparison of activation energies determined using Eq. 11 and from temperature-dependent ASR (Table 1) indicated close matching. These results suggested the charge transfer within the electrode as well as across the electrode–electrolyte interface was via hopping mechanism. Similar results have been reported in literature [10].

Plots of log (ASR) against $10^3/T$ for cells with 70LSM:30GDC composite cathode having LSM prepared using different preparative techniques are depicted in Fig. 9. As seen, the composite with LSM prepared by combustion exhibited lowest ASR and activation energy compared to the other cells under study.

Complex impedance plots of Cell(comb) at 800 °C for different oxygen partial pressures (P_{O_2}), depicted in Fig. 10a, was simulated by two depressed semicircles denoted by dotted lines. Here, also, semicircle corresponding to electrolyte is absent due to high-frequency limit (<1 MHz) of Solartron FRA 1255B. A careful look at the figure revealed that the x-axis intercept

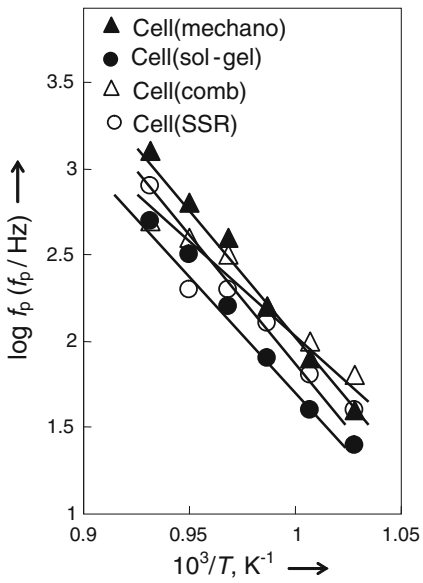

Fig. 8 Arrhenius plots of electrode relaxation frequency obtained for different cells

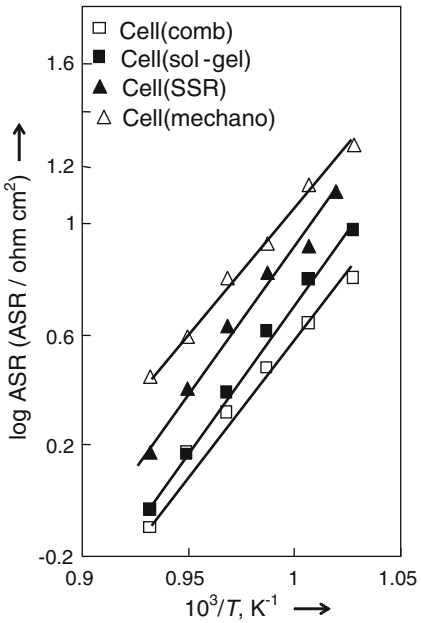

Fig. 9 Arrhenius plots of (ASR) of symmetric cell with cathode prepared by different techniques and sintered at 1,000 °C for 2 h

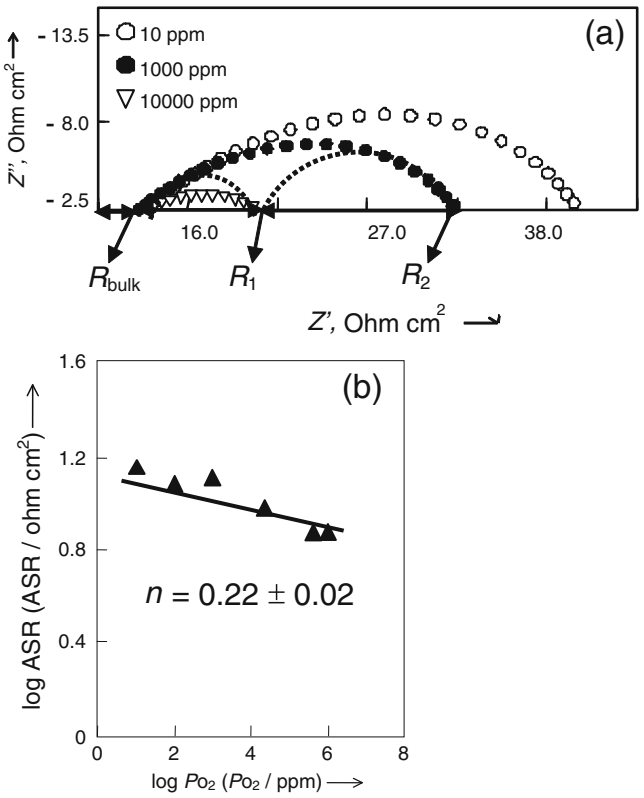

Fig. 10 **a** Complex impedance plots at different oxygen partial pressures for Cell(comb) at 800 °C and **b** variation of ASR with oxygen partial pressure at 800 °C

corresponding to low-frequency semicircular arc changes with change in oxygen partial pressure. On the other hand, electrolytic bulk conductivity is least affected by changes in P_{O_2}. Similar behavior was observed for all cells under study. The variation of ASR with the oxygen partial pressure (Fig. 10b) can be represented by the Eq. 12 given below

$$\mathrm{ASR} = \mathrm{ASR}_0 (P_{O_2})^{-n} \tag{12}$$

The n gives useful information about the type of species involved in the reactions at the electrode [21].

$$n = 1,\ \ O_2(\mathrm{gas}) \rightleftarrows O_{2,\mathrm{ads}} \tag{13}$$

$$n = 0.5,\ \ O_{2,\mathrm{ads}} \rightleftarrows 2O_{\mathrm{ads}} \tag{14}$$

$$n = 0.25,\ \ O_{\mathrm{ads}} + 2e' + V_O^{\bullet\bullet} \rightleftarrows O_O^x \tag{15}$$

$$n = 0,\ O_{\mathrm{TPD}}^{2-} + V_O^{\bullet\bullet} \rightleftarrows O_O^x \tag{16}$$

The n=0.22±0.01 estimated in the present study, indicated adsorption of oxygen in to the lattice giving rise to the electron and the vacancy for oxygen according to relation (15). Van Herle et al. concluded that adsorption has been the rate-limiting mechanism whenever the activation energy of an impedance arc found ≈1 eV [22]. In the present study, the E_a=1.09 eV indicated absorption of O_2 which was the rate-limiting process of cathode. In contrast, reported studies on pure LSM and LSM–YSZ electrodes showed activation energy ≈1.5 eV and the authors concluded that oxygen adsorption and dissociation have been the rate-limiting process/steps. Compared to the platinum electrode, the oxygen reduction on the LSM electrodes was often considered to be more complicated due to oxygen excess non-stoichiometry at high P_{O_2}.

Conclusions

Among all preparative routes, 70LSM:30GDC composite with LSM prepared by combustion technique exhibited lowest ASR (0.70 Ω cm^2) with minimum activation enthalpy (1.093±0.01 eV). The composite exhibited semiconductor behavior up to 680 °C. The mechanochemical synthesis required lowest sintering temperature (700 °C) for the formation of single-phase LSM compared to sol–gel (800 °C), combustion (1,000 °C), and solid-state reaction (1,300 °C). $70La_{0.8}Sr_{0.2}MnO_3$:$30Ce_{0.8}Gd_{0.2}O_2$ composite exhibited good chemical stability. The 70LSM:30GDC

composite with LSM prepared by combustion may be a potential cathode for IT-SOFC applications.

Acknowledgments The authors are thankful to University Grants Commission, New Delhi, for financial support through Special Assistance Program, DRS-II to carry out this work. Ms. K. R. Nagde is grateful to Department of Science and Technology, New Delhi, for the award of Women Scientist Scheme-A (SR/WOS-A/PS-08/2009).

References

1. Singanahally AT, Muthuraraman M, Patil K (1997) J Mater Chem 7(12):2499–2503
2. Hammouche A, Schhouler EJL, Henault M (1988) Solid State Ionics 28:1205–1207
3. Murray EP, Barnett SA (2001) Solid State Ionics 143:265–273
4. Deseure J, Bullet Y, Dessemond L, Siebert E (2005) Electrochim Acta 50:2037–2046
5. Chervin C, Glass RS, Kauzlarich SM (2005) Solid State Ionics 176:17–23
6. Nagde KR, Bhoga SS (2009) Ionics 15:571–578
7. Nagde KR, Bhoga SS (2010) Ionics 16(4):361–370
8. Holland TJB, Redfern SAT (1997) Mineral Mag 61:65–77
9. Kolthoff IM, Elving PJ (1970) Treatise on analytical chemistry. Wiley-Inter science, New York
10. Khandale AP, Bhoga SS (2010) J Power sources 195:7974–7982
11. Harwood MG (1955) Proc Phys Soc 68:586–592
12. Gaudon M, Robert CL, Ansart F, Stevens P, Rousset A (2002) Solid Sate Sci 4:125–133
13. Kuo JH, Anderson HV, Sparlin DM (1990) J Solid State Chem 87:55–60
14. Khandale AP, Bhoga SS (2010) Integr Ferroelectr 116:59–67
15. Tsipis EV, Kharton VV (2008) J Solid State Electrochem 12:1367–1391
16. Chen W, Wen T, Nip H, Zheng R (2003) Mater Res Bull 38:1319–1328
17. Stevenson JW, Nasrallah MM, Anderson HU, Sparlin DM (1993) J Solid State Chem 102:185–197
18. Badwal SPS, Jiang SP, Love J, Nowotny J, Rekas M, Vance ER (2001) Ceram Int 27:431–498
19. Qiang L, Sun LP, Huo L, Zhao H, Grenier J (2011) J Power Sources 196:1712–1716
20. Suzuki T, Awano M, Jasinki P, Prtrovsky V, Anderson HU (2006) Solid State Ionics 177:2071–2074
21. Ping S, Qiang L, Hua H, Hui Z, Ying Z, Nan L, Viricelle J, Pijolat C (2011) J Power Sources 196:5835–5839
22. Van Herle J, Mcevoy AJ, Thampi KR (1996) Electrochim Acta 41:1447–1454